

Article

Bioactivity and Mechanical Properties of Hydroxyapatite on Ti6Al4V and Si(100) Surfaces by Pulsed Laser Deposition

Salizhan Kylychbekov ¹, Yaran Allamyradov ¹, Zikrulloh Khuzhakulov ¹, Inomjon Majidov ¹, Simran Banga ^{2,*} , Justice ben Yosef ³, Liviu Duta ^{4,*}  and Ali Oguz Er ^{1,*}

¹ Department of Physics and Astronomy, Western Kentucky University, Bowling Green, KY 42101, USA; salizhan.kylychbekov837@topper.wku.edu (S.K.); yaran.allamyradov485@topper.wku.edu (Y.A.)

² Department of Biology, Western Kentucky University, Bowling Green, KY 42101, USA

³ Department of Chemistry, Western Kentucky University, Bowling Green, KY 42101, USA

⁴ National Institute for Lasers, Plasma and Radiation Physics, 077125 Magurele, Romania

* Correspondence: simran.banga@wku.edu (S.B.); liviu.duta@inflpr.ro (L.D.); ali.er@wku.edu (A.O.E.)

Abstract: In this study, the effects of substrate temperature and ablation wavelength/mechanism on the structural, mechanical, and bioactivity properties of hydroxyapatite (HA) coatings were investigated. HA coatings were deposited on both Si(100) and Ti6Al4V surfaces. Substrate temperature varied from room temperature to 800 °C. Depositions were performed in Ar/H₂O and vacuum environments. X-ray diffraction, scanning electron microscopy, and atomic force microscopy techniques were used to analyze structural and morphological variations. The adherence of coatings to the substrates was assessed by the pull-out method. The obtained data indicated that with the temperature increase, the coatings steadily crystallized. However, temperatures above 700 °C adversely affected protein adsorption and adhesion properties. Similar trends were confirmed via pull-out testing, protein adsorption, and cell proliferation tests. The ablation mechanism was also proven to play an important role in the deposition process. Overall, this study provides further evidence that crystallinity is a vital factor in the functionality of the coatings and depends on the deposition conditions. However, all measurements directly indicated that beyond 700 °C, the morpho-structural, mechanical, and bioactivity properties degrade.

Keywords: hydroxyapatite coating; pulsed laser deposition; mechanical testing; bioactivity; protein adsorption; surface characterization



Citation: Kylychbekov, S.; Allamyradov, Y.; Khuzhakulov, Z.; Majidov, I.; Banga, S.; ben Yosef, J.; Duta, L.; Er, A.O. Bioactivity and Mechanical Properties of Hydroxyapatite on Ti6Al4V and Si(100) Surfaces by Pulsed Laser Deposition. *Coatings* **2023**, *13*, 1681. <https://doi.org/10.3390/coatings13101681>

Academic Editor: Michał Kulka

Received: 31 August 2023

Revised: 16 September 2023

Accepted: 18 September 2023

Published: 25 September 2023



Copyright: © 2023 by the authors. Licensee MDPI, Basel, Switzerland. This article is an open access article distributed under the terms and conditions of the Creative Commons Attribution (CC BY) license (<https://creativecommons.org/licenses/by/4.0/>).

1. Introduction

Biological responses to materials differ based on the differences in surface and interface properties. Conventional implants are commonly made from three families of metals: 316 L stainless steel, cobalt chromium, and titanium alloys. Although they have excellent tensile strength and stability over long periods, they are biologically inert [1]. Bones, in contrast, participate in vital biological processes in addition to structurally supporting the body. This drawback of metals results in complications with statistically significant effects [2–4]. To improve the biological performance of metal surfaces, multiple alternatives were proposed [5–12]. A good candidate for coatings should possess low degradation, high biocompatibility, antibacterial, and wear resistance properties [13,14]. Among them, coating metal surfaces with calcium phosphates (CaP), specifically with hydroxyapatite (HA, Ca₁₀(PO₄)₆(OH)₂), has been a main topic of interest for the last several decades for clinical applications such as prostheses, orthopedics, drug delivery, and dentistry [15–17]. The global implant market growth has been forecasted at a 6.8% compound annual growth rate (CAGR) for the period between 2022 and 2032 [18]. A similar trend pertains to the global HA market, with USD 2.3 billion in 2023 with a CAGR of 6.52% forecasted for 2023–2028. The main motivation for this industry is that coating the metal surface with CaP allows one to combine the metal's mechanical properties with the biocompatibility of CaP.

HA, being one of the main components of human bones, is biocompatible, bioactive, and thermodynamically stable in body fluid environments [19,20]. It also actively takes part in essential bone regeneration processes by osteogenic stimulation through the release of Ca^{2+} , PO_4^{4-} , and OH^- ions when in contact with blood plasma [21]. Coating the metal surface with HA offers numerous solutions to problems such as metal ion release from the metal surface, foreign body inflammation, and bone cell repair. Research progress has shown that crystalline HA is the most active constituent in human bones and is more stable in human body fluids that contain a variety of dissolving ions [15,21]. Among conventional coating methods, pulsed laser deposition (PLD) has been successful in producing crystalline HA coatings with applicable adhesion strength [22–24].

In addition, PLD can be used to synthesize various materials, including metals and semiconductors [25–30]. PLD is a thin film deposition technique where a high-power pulsed laser beam is focused inside a vacuum chamber to ablate the target of desired composition. Parallel to developments in lasers, PLD has become more popular in current research environments.

However, PLD is notorious for creating particulates during deposition. These droplets could later affect the photoemission performance of photocathodes. Particulate size ranges from the sub-micron level to several micrometers in size [31]. Particulate formation is affected by a number of parameters, such as the target, laser parameters, surface quality, and laser energy density. Multiple alternatives, such as using a shorter pulse width laser, or using bi-directional ablation were proposed to prevent particulate formation in PLD [11,32,33].

It has been reported that unmatched crystallinity and bonding strengths of HA could be obtained using the PLD technique [34]. Although DC Magnetron and RF sputtering have achieved reliable crystallinity, they showed weak adherence between the coating and metal surface [35]. Another widely suggested method is plasma spraying, but it uses high-temperature plasma leading to unwanted phases of CaP such as TTCP, α - and β -TCP, in addition to HA, which emerge at high temperatures [36–38]. In contrast, PLD has been used in the successful production of a variety of crystalline coatings with high adhesivity. Most of the studies reported post-deposition annealing as a necessary step to obtain crystalline coatings [39–43]. However, crystalline coatings at room temperature using a 532 nm Nd:YAG laser at high fluences were reported [44]. It was suggested that high fluences enabled more expelled elements and particulates and provided higher kinetic energy for the plume particles to find ideal nucleation sites. This was an unpredicted result compared to the general trend of using post-deposition annealing at high temperatures and providing enough H_2O vapor during the nucleation phase, as they are known to be critical for the successful production of HA crystals and maintenance of stoichiometry or Ca/P ratio [39–41]. Recently, the trend has shifted towards doped-HA coatings to merge additional functions through nanoparticles and elements such as Zn [45,46], Ag [47,48], F [49], and so forth [23,50,51].

One interesting aspect of PLD is the ablation mechanism. Historically, in the PLD of HA, two pulsed laser systems were used: Nd:YAG and excimer lasers. Nistor et al. [52] have reported coatings with 355 and 532 nm Nd:YAG lasers. Coating with a 532 nm laser produced pure HA phases, but 355 nm consisted of α -TCP and HA [52]. Although the observations are singular, they are relatively comparable. Recently, a Japanese group published several interesting reports on eliminating particulates using the so-called telescope model [53,54]. They reported that crystallinity was also significantly enhanced, as big particulates were unable to cross the obstacle, while atoms, electrons, and ions crossed and nucleated upon reaching the substrate. When considering the excimer system, ArF and KrF lasers were used. They were reported to induce columnar growth. In summary, while no single group studied all ablation systems at once, it is evident that the excimer lasers induce columnar growth while Nd:YAG lasers produce granular growth.

In the current work, we had two aims. Firstly, a complete analysis of substrate temperature effects was performed, as it is not fully understood yet. Although other groups

have briefly touched on this subject, an extensive study with a full range is not yet available. Secondly, complete data on the unified set of Nd:YAG wavelengths: 1064, 532, and 355 nm in a single work was reported. This examination focused on three fronts, i.e., mechanical, morphological, and bioactivity assessments. Bioactivity by itself is a broad term, so the emphasis was placed on in vitro protein adsorption and cell proliferation.

2. Materials and Methods

2.1. Experimental Details

2.1.1. Substrate Preparation

Si(100) wafers and grade 5 Ti6Al4V plates were purchased from mtixtl.com and Titanium Industries Inc. Si(100) arrived with one side already polished, while Ti6Al4V were cut into 15 mm × 15 mm sheets and polished until a 0.05 μm mirror finish was obtained. First, sanding was performed using SiC pads sequentially with grit sizes of 180, 400, 600, and 1000. Then, 0.05 μm colloidal silica/alumina solution and colloidal silica suspension were used simultaneously for fine polishing. Finally, substrates were cleaned for 5 min each in both acetone and deionized water using an ultrasonic bath.

2.1.2. Coating Process

The PLD equipment consisted of the pulsed Nd:YAG nanosecond laser source (Continuum Surelite II), a stainless-steel ultrahigh vacuum chamber equipped with a resistive substrate heater, and a rotating target holder system. The laser had a fundamental wavelength of 1064 nm, a pulse width of 5 ns, a 10 Hz repetition rate, and a Gaussian pulse shape of 6 mm diameter when the beam was unfocused. Harmonic beams with 532 nm and 355 nm wavelengths were generated using KDP crystals. The fluence was adjusted at 7.4 J/cm². The substrate-to-target separation distance was set between 3 and 5 cm. The substrate temperature was varied from room temperature (RT) to 800 °C (i.e., RT, 300, 500, and 800 °C). Depositions were performed in vacuum at 10⁻⁶ Torr and 3.0 × 10⁻¹ Torr water vapor, supplied to the vacuum chamber by bubbling the Ar gas through the water bath at RT. Commercially available HA (3D Biotek, LLC, Bridgewater, NJ, USA) dense discs, 9.5 mm in diameter, 1.6 mm thick, and 1.67 Ca/P ratio, were used as a target material. The targets were rotated at 8 rpm to ensure homogeneous ablation.

2.2. Surface Characterization: SEM, AFM, AmScope

The surface of the coatings was characterized by scanning electron microscopy (SEM), atomic force microscopy (AFM), and optical microscopy techniques. For SEM, a JEOL 6510LV 10–20 kV scanning electron microscope (JEOL Ltd., Tokyo, Japan) was used with energy-dispersive X-ray analysis. Thickness measurements were assessed by cracking the Si(100) sample and loading it vertically upward. The surface roughness measurements were performed with the Nanosurf FlexAFM atomic force microscope (Nanosurf AG, Liestal, Switzerland) operated in contact mode. Quantitative calculations were obtained using Gwyddion software (version 2.62). For bulk analysis, an AmScope optical microscope (United Scope LLC., Irvine, CA, USA) with the model number SM-1TSZZ-144S-10M was used.

2.3. Structural Analysis: XRD, FTIR

Phases of the coatings were identified with a 2nd generation Bruker X-ray Diffraction machine with Cu-Kα radiation source excited at 30 kV X-ray generation voltage and 1.54 Å wavelength. The bonding structure of the HA films was characterized by Fourier-transform infrared spectroscopy (FTIR Perkin Elmer Spectrum 100 (PerkinElmer Inc., Waltham, MA, USA)).

2.4. Mechanical Analysis and Adherence Strength: Pull-Out Tests

The pull-out bonding strength (tensile) at the film-substrate interface is considered of paramount importance in the process of high-quality implant fabrication [55] and the long-term functioning and stability of these medical devices [56] in situ. Thus, it was included

as a quality factor in the International Standard 13779-2/2018 [57], which regulates the fabrication of load-bearing implant coatings.

The adherence of the synthesized HA coatings onto Ti substrates was estimated using the pull-out method. For these tests, a DFD Instruments[®] PATHandy MICRO AT101 (maximum pull force of 1 kN) adherence instrument, equipped with stainless-steel test elements (dollies) with diameters of 0.28 cm, was used. The dollies were glued to the coatings' surface with a special E1100S single-part epoxy glue.

First, the stub surface was polished, then ultrasonically cleaned in acetone and ethanol, and finally dried in nitrogen flow. After gluing, the HA coatings were dried in an oven (at 130 °C for 1 h). Prior to the investigations, three quality tests to control the bonding adhesive strength using uncoated Ti substrates were performed. The mean value of the adhesive strength, measured at the stainless-steel test element-Ti control interface, was 55 ± 4.3 MPa. Each dolly was pulled out vertically using a calibrated hydraulic pump. The extraction force was gradually increased until detachment. For each coating, the measurements were performed on quadruplicates and were in accordance with the ASTM D4541 [58] and ISO 4624 standards [59].

2.5. Biological Assessment

2.5.1. Cell Growth Experiment

HEK 293T cells were maintained in Dulbecco's modified eagle medium supplemented with 10% fetal bovine serum and antibiotics. For the assay, five different disc samples (i.e., control–uncoated and coated at RT, 300, 500, and 800 °C) were placed in 48-well plates in duplicate and seeded with 50,000 cells per well. The samples were incubated at 37 °C in 5% CO₂. At specific time points (i.e., 24, 72, and 120 h), the discs were washed gently with phosphate-buffered saline, and cells were collected to perform a cell count using a counting chamber. The cell counts were analyzed using ANOVA for statistical comparisons between different surfaces at each time point.

2.5.2. Protein Adsorption

Bovine Serum Albumin (BSA) is a relatively small protein with 66 kDa of mass and makes up approximately 60% of all proteins. Albumin is also the most common protein in human blood. Therefore, BSA was chosen for the protein adsorption study.

First, 400 µg/mL of BSA was prepared. HA coatings were submerged in ethanol and flamed for sterilization. Then, triplets from each sample were placed in 48-well plates, and 300 µL of BSA was added onto each sample. Every 24 h, 25 µL of BSA solution was taken from each sample and placed in a 96-well plate and examined under UV-Vis spectroscopy. For quantization, a Pierce[™] Protein Assay Kit was used. Optical Density was measured at 562 nm, and protein concentration in the liquid was calculated accordingly.

3. Results and Discussion

While multiple synthesis conditions affect the ablation process, one of the most significant conditions is the wavelength of the laser pulse. When the wavelength is shorter, the photon energies increase, allowing for bond breakage within the atomic lattice, thereby resulting in ionization [60]. This leads to the ejection of atoms and ions without resulting in adverse heating effects. Shorter wavelengths also result in shallower laser penetration depths and, therefore, lower the threshold fluences and ablation rates. In contrast, longer wavelengths often yield higher densities and larger sizes of particulates and/or droplets. Infrared or visible laser light usually processes materials by producing intense local heating that can melt or vaporize the material, which may cause serious damage to surrounding areas. This contributes to stronger compositional deviations in the film [61]. Therefore, UV irradiation at shorter wavelengths typically yields lower amounts of nano/microparticles as compared to irradiation at longer wavelengths.

During the ablation process, micro to nanostructures are frequently formed on the surface of the target material. These structures increase the surface area and, in turn, reduce

the effective laser fluence. It has been reported that the wavelength of the laser pulse affects the size and frequency of the periodic structures that appear on the target surface [62]. Moreover, the wavelengths not only impact the absorption by the target material but also influence the absorption by the laser-generated plasma plume [61,63].

The useful range of laser wavelengths for ablation typically falls between 200 and 400 nm. Excimer lasers are often preferred for ablation due to their higher energies and relatively flat top energy profile. In contrast, Nd:YAG lasers demonstrate a Gaussian energy profile. Therefore, the variation in fluence inherent to the Gaussian profile must be considered when determining deposition parameters if using a Nd:YAG laser [64]. The ablation mechanism in PLD of HA with 532 nm using fast-gated ICCD cameras and spatio-temporal spectroscopic tools was studied. It was therefore reported that the plasma plume consisted of droplets, atoms, and ions-electrons [65].

While atoms and ions nucleate at the surface, droplets cause hardships in the seeding process. Therefore, minimizing amounts of droplets could enhance the crystallinity of the films [53,54].

Temperature is also known to affect many properties of the film during and after deposition. At higher temperatures, adatoms on the substrate's surface gain thermal energy, and surface diffusion is enhanced, thus promoting crystal growth. The transition from a textured microstructure to a densely packed crystal structure occurs over a range of temperatures.

To study the effect of wavelength and temperature, HA coatings were grown at three different wavelengths (i.e., 1064, 532, and 355 nm) and various temperatures (i.e., RT, 500, and 800 °C). The SEM images from Figure 1 show the clear effect of the temperature and wavelength.

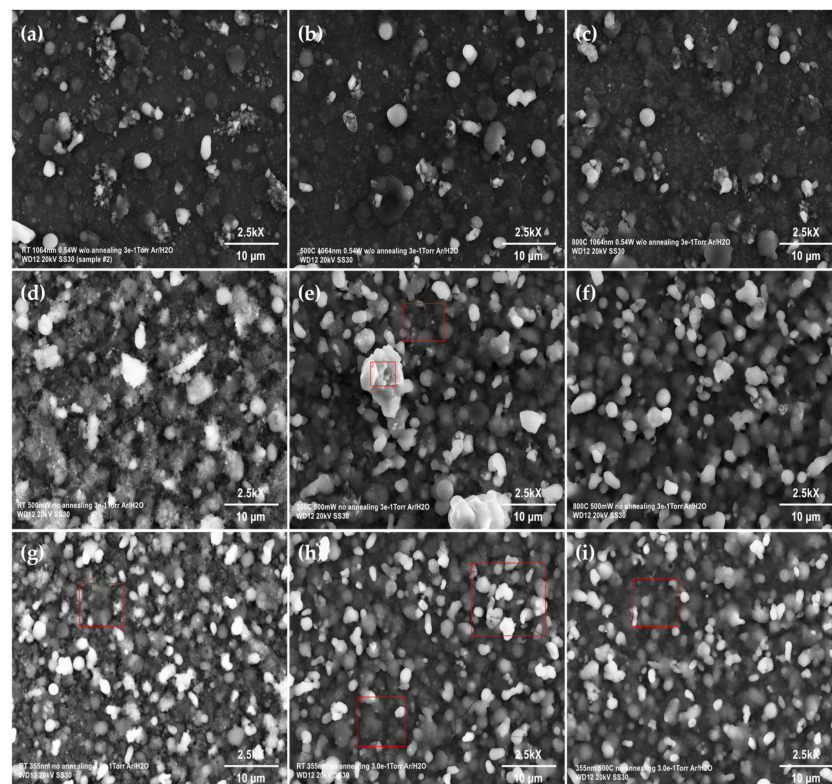


Figure 1. SEM images of hydroxyapatite coatings deposited at 1064 nm (a–c), 532 nm (d–f), and 355 nm (g–i) laser wavelengths at three different substrate temperatures: room temperature, 500 °C, and 800 °C. The red squares indicate the areas for which EDS analysis was performed.

As the wavelength increased from 355 to 1064 nm, the roughness of the coatings also increased. In addition, surface roughness initially increased when the temperature was

raised from RT to 800 °C, but the magnitude of the increase between 500 °C and 800 °C is smaller as compared to the change between RT and 300 °C. The red squares on the SEM micrographs indicate the areas for which EDS analysis was performed. Based on the results, brighter particulates and the background had a similar Ca/P ratio.

Extensive EDS analysis was performed to understand the deposition stoichiometry, i.e., the Ca/P ratio. Results are provided in Supplementary Materials attached as Figures S4–S6. The first notable observation was that as the substrate temperature was raised, the Ca/P ratio increased in all wavelength regimes. A similar behavior was observed before by ArF excimer laser deposition, and their FTIR spectroscopic analysis revealed that PO_4^{4-} groups were gradually replaced with CO_3^{2-} groups as the temperature increased [66]. This result was also supported by our XPS measurements confirming the abundance of C1s excitations at higher temperatures.

Another observation point on the EDS analysis was about the effect of ablation wavelengths on the Ca/P ratio. 1064 nm and 532 nm produced HA coatings were had Ca/P ratios in the 1.6–1.7 range, while the 355 nm beam produced coatings with a Ca/P ratio higher than 1.7, for all substrate temperatures. Previously, Nistor et al. [52] reported that when identical deposition parameters were used but with two different wavelengths of 532 and 355nm, 355 nm one led to a smoother surface with non-HA phases [52]. Although it is not exactly known through which mechanism the stoichiometry is changing, it shows that one can get different stoichiometry and surface microstructures by varying the ablation wavelength.

Figure 2 shows the cross-sectional SEM image of HA coatings synthesized at 1064 nm. One can observe that an increase in the deposition temperature caused an increase in the surface roughness. With the temperature increase, the surface morphology became coarser due to faster surface-mass transport.

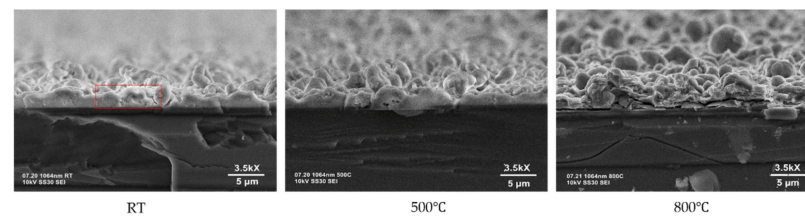


Figure 2. Cross-sectional view vs. substrate temperature in the case of hydroxyapatite coatings deposited at 1064 nm.

Figure 3 shows the cross-sectional view of SEM images of the deposited HA coatings at different wavelengths, along with the AFM line scan. From the cross-sectional view, one can observe that at 800 °C, the HA coating's microstructure is fragile. This effect had consequences that can be seen in protein adsorption, cell growth, and adherence strength tests. At this interface, the EDS results also suggested a lower Ca/P ratio, showing that the stoichiometry was not completely maintained, indicating some signs of degradation.

Another important aspect is the deposition rate. Among the three wavelengths, 532 nm gave the highest yield with 97.5 nm/min, then 355 nm with 38.5 nm/min, and 1064 nm had the lowest rate of 25.7 nm/min. It is understandable that the absorption wavelength of bulk hydroxyapatite is in the range of 300–500 nm; therefore, 532 nm had the better absorption, leading to a higher yield. However, when compared to Nd:YAG lasers, excimer lasers have relatively higher yields because of their repetition rate and flat-top pulse shape.

The AFM lines scan measurements indicated that the roughness values of the HA coatings increased with the used wavelength. When 355 nm was applied, RMS values of $0.65 \pm 0.01 \mu\text{m}$ were inferred. RMS values increased to $1.01 \pm 0.01 \mu\text{m}$ (for 532 nm) and $1.02 \pm 0.01 \mu\text{m}$ (for 1064 nm). This result confirmed previous reports conducted at the same wavelength [44].

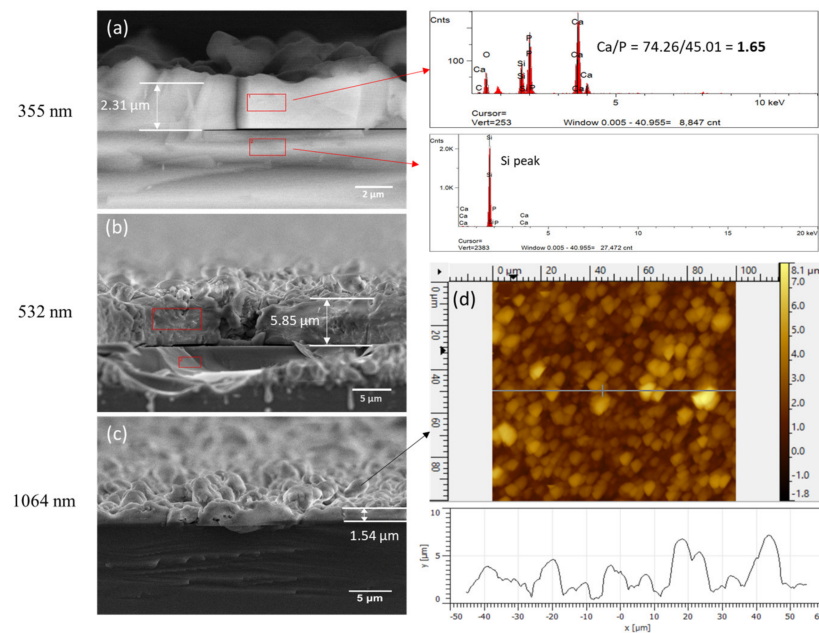


Figure 3. Cross-sectional SEM images of HA coatings deposited with (a–c) 355, 532, and 1064 nm laser beams. (d) AFM profile of (c).

Figure 4 shows the XRD peaks obtained at three different surface temperatures on Ti substrates (JCPDS 09-0432). At RT, two small peaks start to appear around $\theta = 32^\circ$. As the temperature increases, additional peaks appear, and the crystallinity of the sample increases with those additional peaks. At 800 °C, the XRD image shows extra peaks corresponding to tetracalcium phosphate (TTCP) in addition to the additional peaks of HA coatings. A small shift in the Ti substrate XRD peaks was observed. The apparent shift in the Ti substrate could be due to residual, thermal, and epitaxial strain. In addition, thermal strain may play a role due to variations in the cell parameters because of substrate and coating having different thermal expansion coefficients. In addition, some residual strain induced by the laser-ablated high-energy particle impingement may cause intrinsic residual strain, which may result in a slight change of XRD peaks of the substrate.

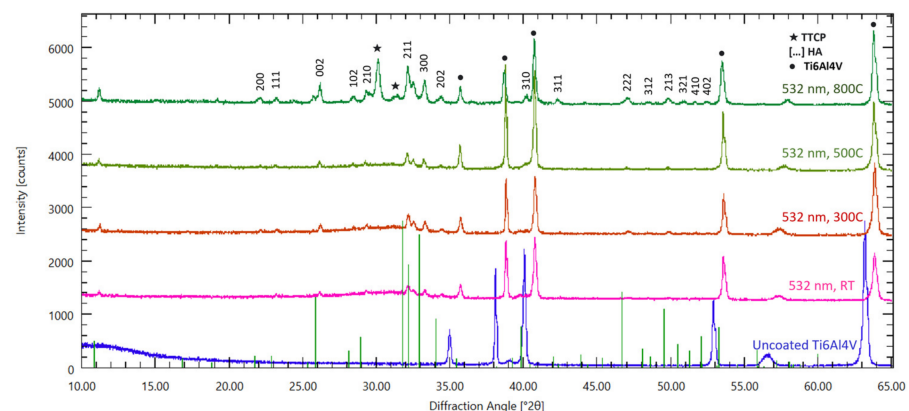


Figure 4. X-ray diffractograms of hydroxyapatite coatings synthesized onto Ti6Al4V substrates using a 532 nm beam. Referenced to JCPDS 09-0432.

The XRD images of HA coatings deposited onto Si(100) substrates are presented in Figure 5 (JCPDS 09-0432). The peak structure follows an analogous trend as in the case of HA coatings on Ti substrates. Similar to the case of HA coatings on Ti6Al4V, TTCP peaks emerged at 800 °C. It can, therefore, be concluded that temperature is a critical factor when synthesizing crystalline HA coatings on different types of substrates.

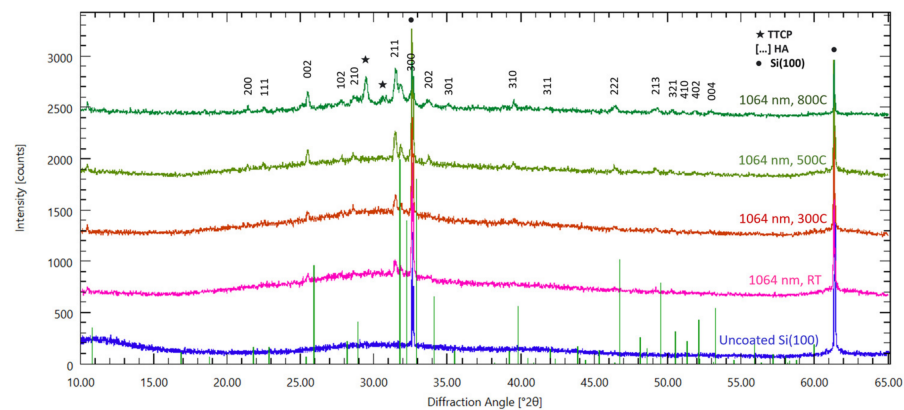


Figure 5. HA on Si(100) deposited with a 1064 nm beam. Referenced to JCPDS 09-0432.

Previously, it was demonstrated that the substrate temperature is a critical factor in determining the phase of the NbN_x and Pb films. For a substrate temperature up to 450 °C, the film showed poor crystalline quality [17]. With temperature increase, the film became textured, and for a substrate temperature of 650–850 °C, a mix of cubic NbN and hexagonal phases was formed, and the surface roughness of the NbN_x films increased as the temperature was raised from 450 °C to 850 °C. For Pb films, it was shown that when the substrate temperature was raised from RT to 300 °C, the film growth mechanism changed from Volmer-Weber to cluster formation mode. When the temperature was raised to values close to the melting temperature of Pb, the Ostwald ripening effect was observed [67]. In our case, the melting temperature of HA was far from the substrate temperature range; however, the results suggest that the variations in substrate temperature affected the nucleation-growth process, allowing smaller particles to conglomerate and possibly form larger crystals. The conglomeration process and growth of hexagonal-shaped crystals were observed at the powder-pellet level, further confirming the observations. As shown in Figures S2 and S3 in the Supplementary Materials, the crystal sizes steadily got bigger as the temperature was raised from 800 °C to 1200 °C, and crystallites melted at 1400 °C, at the temperature above the melting point of HA.

To estimate the change of crystallinity during various substrate temperatures, the crystallinity index (CI (%)) was calculated. The XRD deconvolution method was used for this purpose because it leads to more accurate values as compared to the easier and more popular Segal method [68]. The deconvolution of the X-ray diffraction patterns was performed with Origin Pro 2023b software, considering the Gaussian function as the shape of the resolved peaks. First, XRD patterns were baseline-corrected with user-defined points. Then, the CI (%) was calculated according to the following relation:

$$CI(\%) = \frac{S_c}{S_t} \times 100\%$$

where S_c is the area of the crystalline domain, and S_t is the area under a total domain (crystalline and amorphous). The domain of the crystalline peak was identified according to FWHM.

The CI (%) values for the coatings deposited on Ti6Al4V were as follows: RT (16.6%), 300 °C (32.7%), 500 °C (51.1%), and 800 °C (81.5%). The CI (%) values for the coatings deposited on Si(100) were relatively lower: RT (6.2%), 300 °C (12.0%), 500 °C (32.1%), and 800 °C (61.4%). Corresponding calculations are provided in Figure S1 in the Supplementary Materials. In both cases, the crystalline-to-amorphous ratio steadily grew with respect to the substrate temperature.

It is important to note that the peaks of Si(100)-grown HA were shifted to lower angles, while the ones corresponding to Ti6Al4V-grown HA were shifted to higher angles. In principle, left-shift in XRD means lattice relaxation, while right-shift implies lattice strain. However, in the current situation, it is systematic, regardless of the applied temperatures.

Therefore, the origin of this effect is not evident. This imminent effect suggests an epitaxial-like behavior, but it does not follow the substrate crystal structure one-to-one. Murphy et al. [69] advanced an interesting observation regarding this issue. According to their results, once the initial layer of HA seeds, it grows identically regardless of the substrate. Therefore, the initial seeding process is determined by the substrate's thermodynamics, and the remaining growth process follows the primary nucleation regardless of the substrate structure.

The amorphous material lacks a long-range order, and XRD of amorphous materials has a broad hump, and sharp diffraction peaks are absent. Our results show that the HA coating is mostly crystalline, as confirmed by the presence of sharp diffraction peaks.

Coating Adherence

From a macroscopic point of view, all synthesized HA coatings were adherent to the Ti substrates, as demonstrated by preliminary adherence tests such as the finger test and application/removal of an adhesive tape (i.e., scotch test).

The measured values of adherence of the HA coatings synthesized by PLD at various substrate temperatures, i.e., RT–800 °C, are presented comparatively in Figure 6 and were calculated as mean \pm standard deviation (SD). It should be emphasized that the events were considered only if the fracturing was of an adhesive type, i.e., when it occurred at the coatings-Ti substrate interface.

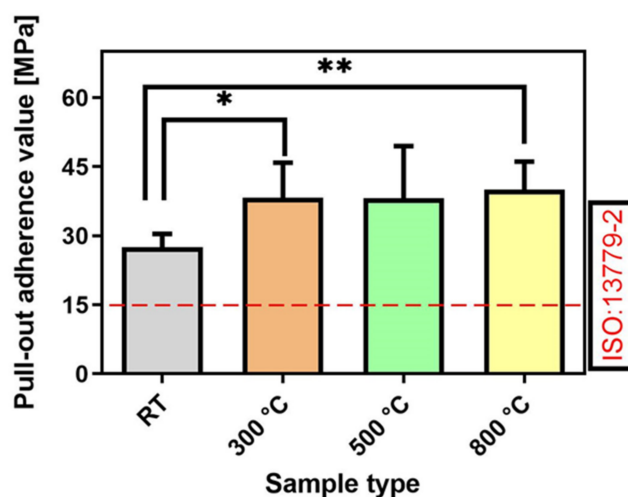


Figure 6. Mean bonding strength adherence values obtained in the case of hydroxyapatite coatings synthesized by pulsed laser deposition onto titanium substrates at RT, 300 °C, 500 °C, and 800 °C. Note: * $p < 0.05$, and ** $p < 0.01$, Student's *t*-test.

The pull-out test results (Figure 6) indicated dissimilar performances of the HA coatings fabricated at different substrate temperatures. HA coatings synthesized at RT were cleanly detached from the Ti substrate, yielding bonding strength values of ~27 MPa. The increase in the substrate deposition temperature seemed to result in an improvement in the films' adherence to the Ti substrate (Figure 6). Thus, in the case of HA coatings deposited at (300–800) °C, the pull-out detachment values were superior to the ones inferred for RT-synthesized coatings, being situated in a narrow range of 38–40 MPa.

The decreased value of the bonding strength inferred for HA coatings synthesized at RT could relate to a larger content of the amorphous counterpart, evident in this specific case using XRD. From the results presented in Figure 6, it can be observed that the highest values of adherence corresponded to the HA coatings fabricated at 800 °C. This trend is similar to those previously reported in the literature for biological-origin HA coatings fabricated by PLD [22–24,70].

It is also important to note that only adherence values higher than the threshold imposed by ISO-137792 Part 2 Standard (i.e., >15 MPa) are considered acceptable for the coatings intended for applications with high biomechanical loads. Considering this criterion, the adherence values measured in the case of HA coatings (~three times higher than the threshold) should be emphasized.

Protein adsorption is a fundamental step in the interaction between cells and surface systems. When a biomaterial is exposed to biological fluids or tissues, proteins in the surrounding environment quickly adsorb onto its surface. The adsorbed proteins form a dynamic interface through noncovalent bonding that mediates subsequent cellular responses and influences the material's biocompatibility, which might be caused by the charged surface of the HA [71]. The adsorption of the protein to HA depends on the charged state of the surface. Given that we have a polycrystalline state, as is evident from the XRD image, the surface has multiple axis directions of domains. It is, therefore, expected that a positively charged surface (a-axis oriented domain) and a negatively charged surface (c-axis oriented domain) adsorb biological molecules such as carboxyl groups, phosphate groups, amino acids with charged side chains, and other charged particles.

We have measured the protein desorption of HA on Ti surface to evaluate its stability, as shown in Figure 7. Our results present that Ti with HA coatings shows better stability compared to a Ti-only surface. When the deposition temperature was situated between RT and 500 °C, no significant change in the protein desorption was observed. However, when the temperature was further increased to 800 °C, the protein desorption rate increased. It is normally expected that protein desorption should be the lowest at 800 °C due to its multiple peaks. However, it should be noted that the surface of the coating at 800 °C is quite coarse. In addition, surface roughness initially increases when the temperature is increased from RT to 800 °C, but the change in the increase between 500 °C and 800 °C is smaller compared to the change between RT and 300 °C.

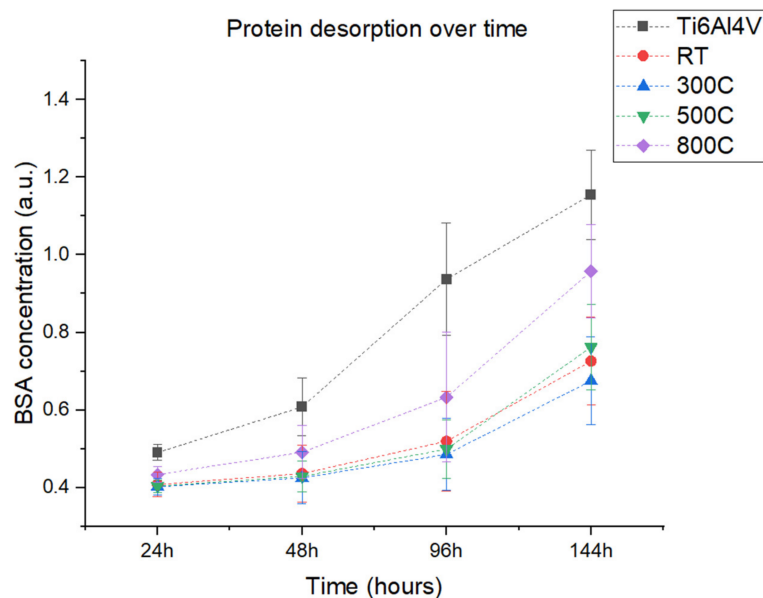


Figure 7. Protein desorption over time on the Ti6Al4V surface and hydroxyapatite coatings deposited at room temperature, 300 °C, 500 °C, and 800 °C.

Patterned surfaces have been shown to decrease the surface attachment of numerous microorganisms and to reduce the biofilm formation [11,72]. In the case of rough surfaces, the surface area of each island increases, which may lead to a decrease in the bonding site and the accessibility to the potential attachment sites, which leads to an energetically unstable surface to which biological molecules are unable to form a stable attachment.

As the wavelength increases from 355 to 1064 nm, the roughness of the film increases. Therefore, it is expected that there will be less protein absorption on the 1064 nm surface compared to the 355 nm surface. This is also in agreement with the observation of a higher number of peaks for the 532 nm samples, which have a higher protein absorption compared to 1064 nm.

It should be noted that there are many factors influencing the interaction between proteins and the HA surface, such as protein structures, morphology of HA surfaces, surroundings, and so on. Therefore, the interaction mechanism for various proteins might be different from each other.

A cell proliferation assay was performed to analyze the growth of mammalian cells on Ti6Al4V and HA-coated implant surfaces sintered at various temperatures. Our data shows that HA-coated surfaces support significantly more cells over a period of five days. Furthermore, an increase in temperature improves the biological activity of the HA-coated implants, as depicted in Figure 8.

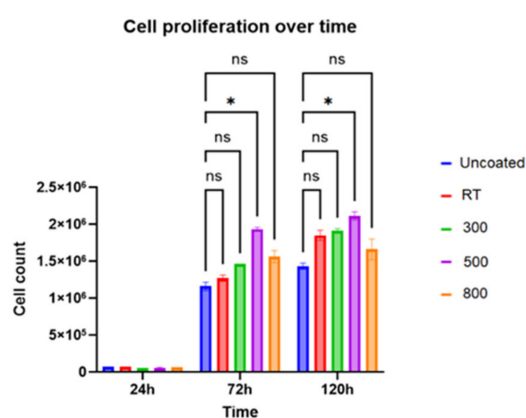


Figure 8. Proliferation of HEK293T cells on the Ti6Al4V substrate and hydroxyapatite coatings deposited at different temperatures with statistically significant (*) and no significance (ns).

One can observe from Figure 8 that the cell proliferation was significantly higher for all HA coatings and improved with the increase in the applied temperature, from RT to 500°C. As observed with protein absorption, higher temperature treatment performed at 800°C did not enhance the cell proliferation further, but it was significantly higher than the uncoated, bare Ti surfaces.

One should note that, for practical applications, the investigation of the long-term stability of HA coatings in model biofluids is of key importance and has to be considered in future studies.

4. Conclusions

HA coatings were grown onto silicon and titanium substrates using pulsed laser deposition (PLD) technique. The depositions were carried out at different surface temperatures and wavelengths. The effects of substrate temperature and ablation wavelength/mechanism on the structural, mechanical, and bioactivity properties of HA coatings were investigated using surface characterization tools, pull-out tests, and cell proliferation assays. Our results indicate that both surface temperature and wavelength are critical factors to obtain crystalline HA coatings. In addition, PLD was shown to be a feasible method to obtain HA coatings for the purpose of bioactivity measurements. The obtained results demonstrated that as the temperature increased, the coatings steadily crystallized. Further increase in the temperature above 700 °C adversely affected protein adsorption and mechanical properties. Similar trends were confirmed via cross-sectional SEM, pull-out testing, and cell proliferation tests performed on the HA coatings.

Supplementary Materials: The following supporting information can be downloaded at <https://www.mdpi.com/article/10.3390/coatings13101681/s1>, Figure S1. Representative calculations of crystallinity indices for (a,b) HA on Ti6Al4V at 800°C and (c,d) HA on Si(100) at deposited RT. Crystallinity index: $CI(\%) = (S_c/S_t) \times 100\%$. Figure S2. SEM images of the HA pellets cold-pressed at 5000 psi, then annealed at different temperatures: (a) amorphous, (b) 800 °C, (c) 1000 °C, (d) 1200 °C, and (e) 1400 °C. Figure S3. XRD patterns of pellets shown in Figure S1. Figure S4. 1064 nm deposition, Ca/P ratio study through EDS analysis. Figure S5. 532 nm deposition, Ca/P ratio study through EDS analysis. Figure S6. 355 nm deposition, Ca/P ratio study through EDS analysis. Figure S7. XPS of HA coating on Ti6Al4V deposited at 500 °C with 532 nm beam.

Author Contributions: Conceptualization, A.O.E.; methodology, A.O.E.; formal analysis, S.K., Z.K., I.M., J.b.Y., S.B., Y.A., L.D. and A.O.E.; investigation, S.K., L.D. and A.O.E.; writing—original draft preparation, S.K. and A.O.E.; writing—review and editing, S.K., Z.K., I.M., J.b.Y., S.B., Y.A., L.D. and A.O.E.; supervision, A.O.E.; project administration, A.O.E. and L.D.; funding acquisition, A.O.E. and L.D. All authors have read and agreed to the published version of the manuscript.

Funding: This research was funded by KY IDEa Networks of Biomedical Research Excellence (ULRF12-1493C-01 via NIGMS grant# 8P20GM103436), KY NSF EPSCoR RA (3048115832-23-186) and RIE (3048115483-22-208), and WKU Research Foundation, Romanian Ministry of Research, Innovation, and Digitization under the Romanian National Core Program LAPLAS VII—contract no. 30N/2023.

Institutional Review Board Statement: Not applicable.

Informed Consent Statement: Not applicable.

Data Availability Statement: Not applicable.

Acknowledgments: We would like to thank John Andersland for SEM measurements.

Conflicts of Interest: The authors declare no conflict of interest.

References

1. Breime, H.; Biehl, V.; Reger, N.; Gawalt, E. Chapter 1a Metallic Biomaterials: Introduction. In *Handbook of Biomaterial Properties*; Springer: Berlin/Heidelberg, Germany, 2016; pp. 151–158.
2. Zhang, D.; Chen, Q.; Shi, C.; Chen, M.; Ma, K.; Wan, J.; Liu, R. Dealing with the Foreign-Body Response to Implanted Biomaterials: Strategies and Applications of New Materials. *Adv. Funct. Mater.* **2020**, *31*, 2007226. [[CrossRef](#)]
3. Espallargas, N.; Torres, C.; Muñoz, A. A metal ion release study of CoCrMo exposed to corrosion and tribocorrosion conditions in simulated body fluids. *Wear* **2015**, *332–333*, 669–678. [[CrossRef](#)]
4. Manivasagam, G.; Dhinasekaran, D.; Rajamanickam, A. Biomedical Implants: Corrosion and its Prevention—A Review. *Recent Patents Corros. Sci.* **2010**, *2*, 40–54. [[CrossRef](#)]
5. Wang, Q.; Wang, W.; Li, Y.; Li, W.; Tan, L.; Yang, K. Biofunctional magnesium coating of implant materials by physical vapour deposition. *Biomater. Transl.* **2021**, *2*, 248–256. [[PubMed](#)]
6. Harun, W.S.; Asri, R.I.; Sulong, A.B.; Ghani, S.A.; Ghazalli, Z. Hydroxyapatite-Based Coating on Biomedical Implant. *Hydroxyapatite Adv. Compos. Nanomater. Biomed. Appl. Its Technol. Facet.* **2018**, 6988. [[CrossRef](#)]
7. Asri, R.I.M.; Harun, W.S.W.; Samykano, M.; Lah, A.N.C.; Ghani, S.A.C.; Tarlochan, F.; Raza, M.R. Corrosion and surface modification on biocompatible metals: A review. *Mater. Sci. Eng. C* **2017**, *77*, 1261–1274. [[CrossRef](#)] [[PubMed](#)]
8. Li, Y.; Yang, W.; Li, X.; Zhang, X.; Wang, C.; Meng, X.; Pei, Y.; Fan, X.; Lan, P.; Wang, C.; et al. Improving Osteointegration and Osteogenesis of Three-Dimensional Porous Ti6Al4V Scaffolds by Polydopamine-Assisted Biomimetic Hydroxyapatite Coating. *ACS Appl. Mater. Interfaces* **2015**, *7*, 5715–5724. [[CrossRef](#)]
9. Li, Y.; Jahr, H.; Zhou, J.; Zadpoor, A.A. Additively manufactured biodegradable porous metals. *Acta Biomater.* **2020**, *115*, 29–50. [[CrossRef](#)]
10. Luo, Y.; Wang, J.; Ong, M.T.; Yung, P.S.; Wang, J.; Qin, L. Update on the research and development of magnesium-based biodegradable implants and their clinical translation in orthopaedics. *Biomater. Transl.* **2021**, *2*, 188–196.
11. Khuzhakulov, Z.; Kylychbekov, S.; Allamyradov, Y.; Majidov, I.; Ben Yosef, J.; Er, A.Y.; Kitchens, C.; Banga, S.; Badarudeen, S.; Er, A.O. Formation of picosecond laser-induced periodic surface structures on steel for knee arthroplasty prosthetics. *Front. Met. Alloy.* **2023**, *1*, 1090104. [[CrossRef](#)]
12. Papynov, E.K.; Shichalin, O.O.; Belov, A.A.; Buravlev, I.Y.; Mayorov, V.Y.; Fedorets, A.N.; Buravleva, A.A.; Lembikov, A.O.; Gritsuk, D.V.; Kapustina, O.V.; et al. CaSiO₃-HAp Metal-Reinforced Biocomposite Ceramics for Bone Tissue Engineering. *J. Funct. Biomater.* **2023**, *14*, 259. [[CrossRef](#)] [[PubMed](#)]
13. Dong, J.; Zhong, J.; Hou, R.; Hu, X.; Chen, Y.; Weng, H.; Zhang, Z.; Liu, B.; Yang, S.; Peng, Z. Polymer bilayer-Micro arc oxidation surface coating on pure magnesium for bone implantation. *J. Orthop. Transl.* **2023**, *40*, 27–36. [[CrossRef](#)] [[PubMed](#)]

14. Guo, Y.; Chen, C.; Zhang, S.; Ren, L.; Zhao, Y.; Guo, W. Mediation of mechanically adapted TiCu/TiCuN/CFR-PEEK implants in vascular regeneration to promote bone repair in vitro and in vivo. *J. Orthop. Transl.* **2022**, *33*, 107–119. [[CrossRef](#)] [[PubMed](#)]
15. Fiume, E.; Magnaterra, G.; Rahdar, A.; Verné, E.; Bairo, F. Hydroxyapatite for Biomedical Applications: A Short Overview. *Ceramics* **2021**, *4*, 542–563. [[CrossRef](#)]
16. Pajor, K.; Pajchel, L.; Kolmas, J. Hydroxyapatite and Fluorapatite in Conservative Dentistry and Oral Implantology—A Review. *Materials* **2019**, *12*, 2683. [[CrossRef](#)] [[PubMed](#)]
17. Ielo, I.; Calabrese, G.; De Luca, G.; Conoci, S. Recent Advances in Hydroxyapatite-Based Biocomposites for Bone Tissue Regeneration in Orthopedics. *Int. J. Mol. Sci.* **2022**, *23*, 9721. [[CrossRef](#)]
18. Medical Implants Market Size to Surpass US\$ 145.6 Bn by 2030. Available online: <https://www.precedenceresearch.com/press-release/medical-implants-market> (accessed on 28 August 2023).
19. Kim, H.; Camata, R.P.; Vohra, Y.K.; Lacefield, W.R. Control of phase composition in hydroxyapatite/tetracalcium phosphate biphasic thin coatings for biomedical applications. *J. Mater. Sci. Mater. Med.* **2005**, *16*, 961–966. [[CrossRef](#)]
20. Klein, C.P.; de Blicq-Hogemrst, J.; Wolket, J.; de Groot, K. Studies of the solubility of different calcium phosphate ceramic particles in vitro. *Biomaterials* **1990**, *11*, 509–512. [[CrossRef](#)]
21. Sobczak-Kupiec, A.; Drabczyk, A.; Florkiewicz, W.; Głab, M.; Kudłacik-Kramarczyk, S.; Słota, D.; Tomala, A.; Tyliczszak, B. Review of the Applications of Biomedical Compositions Containing Hydroxyapatite and Collagen Modified by Bioactive Components. *Materials* **2021**, *14*, 2096. [[CrossRef](#)]
22. Duta, L.; Stan, G.E.; Popescu-Pelin, G.; Zgura, I.; Anastasescu, M.; Oktar, F.N. Influence of Post-Deposition Thermal Treatments on the Morpho-Structural, and Bonding Strength Characteristics of Lithium-Doped Biological-Derived Hydroxyapatite Coatings. *Coatings* **2022**, *12*, 1883. [[CrossRef](#)]
23. Mihailescu, N.; Stan, G.; Duta, L.; Chifiriuc, M.C.; Bleotu, C.; Sopronyi, M.; Luculescu, C.; Oktar, F.; Mihailescu, I. Structural, compositional, mechanical characterization and biological assessment of bovine-derived hydroxyapatite coatings reinforced with MgF₂ or MgO for implants functionalization. *Mater. Sci. Eng. C* **2016**, *59*, 863–874. [[CrossRef](#)] [[PubMed](#)]
24. Duta, L.; Oktar, F.; Stan, G.; Popescu-Pelin, G.; Serban, N.; Luculescu, C.; Mihailescu, I. Novel doped hydroxyapatite thin films obtained by pulsed laser deposition. *Appl. Surf. Sci.* **2013**, *265*, 41–49. [[CrossRef](#)]
25. Er, A.O.; Ren, W.; Elsayed-Ali, H.E. Low temperature epitaxial growth of Ge quantum dot on Si(100)-(2 × 1) by femtosecond laser excitation. *Appl. Phys. Lett.* **2011**, *98*, 013108. [[CrossRef](#)]
26. Farha, A.H.; Er, A.O.; Ufuktepe, Y.; Myneni, G.; Elsayed-Ali, H.E. Effects of substrate temperature on properties of NbN_x films grown on Nb by pulsed laser deposition. *Appl. Surf. Sci.* **2011**, *258*, 1613–1618. [[CrossRef](#)]
27. Er, A.O.; Elsayed-Ali, H.E. Excitation-Induced Germanium Quantum Dot Formation on Si(100)-(2 × 1). *J. Appl. Phys.* **2010**, *108*, 034303–034310. [[CrossRef](#)]
28. Wang, X.; Jiang, J.; Tian, Y. A Review on Macroscopic and Microstructural Features of Metallic Coating Created by Pulsed Laser Material Deposition. *Micromachines* **2022**, *13*, 659. [[CrossRef](#)] [[PubMed](#)]
29. Er, A.O.; Elsayed-Ali, H.E. Femtosecond pulsed laser deposition of Ge quantum dot growth on Si (100)-(2 × 1). *Appl. Surf. Sci.* **2011**, *257*, 8078–8084. [[CrossRef](#)]
30. Er, A.O.; Elsayed-Ali, H.E. Electronically enhanced surface diffusion during Ge growth on Si(100). *J. Appl. Phys.* **2011**, *109*, 084320–084326.
31. Koren, G.; Gupta, A.; Baseman, R.J.; Lutwyche, M.I.; Laibowitz, R.B. Laser wavelength dependent properties of YBa₂Cu₃O_{7-d} thin films deposited by laser ablation. *Appl. Phys. Lett.* **1989**, *55*, 2450–2452. [[CrossRef](#)]
32. György, E.; Mihailescu, I.N.; Kompitsasa, M.; Giannoudakosa, A. Particulates generation and solutions for their elimination in pulsed laser deposition. *J. Optoelectron. Adv. Mater.* **2004**, *6*, 39–46.
33. Mihailescu, I.N.; Teodorescu, V.S.; Gyorgy, E.; Luches, A.; Perrone, A.; Martino, M. About the nature of particulates covering the surface of thin films obtained by reactive pulsed laser deposition. *J. Phys. D Appl. Phys.* **1998**, *31*, 2236–2240. [[CrossRef](#)]
34. Hontsu, S. Preparation of Biomaterial Thin Films by Pulsed-Laser Deposition Technique. *Rev. Laser Eng.* **2000**, *28*, 407–412. [[CrossRef](#)]
35. Oladijo, S.; Akinlabi, E.; Mwema, F.; Stamboulis, A. An Overview of Sputtering Hydroxyapatite for Biomedical Application. In *IOP Conference Series: Materials Science and Engineering*; IOP Publishing: Bristol, UK, 2021.
36. Sun, L.; Berndt, C.C.; Gross, K.A.; Kucuk, A. Material fundamentals and clinical performance of plasma-sprayed hydroxyapatite coatings: A review. *J. Biomed. Mater. Res. Off. J. Soc. Biomater. Jpn. Soc. Biomater. Aust. Soc. Biomater. Korean Soc. Biomater.* **2001**, *58*, 570–592. [[CrossRef](#)] [[PubMed](#)]
37. Cheang, P.; Khor, K. Addressing processing problems associated with plasma spraying of hydroxyapatite coatings. *Biomaterials* **1996**, *17*, 537–544. [[CrossRef](#)] [[PubMed](#)]
38. Massaro, C.; Baker, M.A.; Cosentino, F.; Ramires, P.A.; Klose, S.; Milella, E. Surface and biological evaluation of hydroxyapatite-based coatings on titanium deposited by different techniques. *J. Biomed. Mater. Res. Off. J. Soc. Biomater. Jpn. Soc. Biomater. Aust. Soc. Biomater. Korean Soc. Biomater.* **2001**, *58*, 651–657. [[CrossRef](#)] [[PubMed](#)]
39. Cotell, C.M.; Chrisey, D.B.; Grabowski, K.S.; Sprague, J.A.; Gossett, C.R. Pulsed laser deposition of hydroxylapatite thin films on Ti-6Al-4V. *J. Appl. Biomater.* **1992**, *3*, 87–93. [[CrossRef](#)]
40. Baeri, P.; Torrisi, L.; Marino, N.; Foti, G. Ablation of hydroxyapatite by pulsed laser irradiation. *Appl. Surf. Sci.* **1992**, *54*, 210–214. [[CrossRef](#)]

41. Dinda, G.; Shin, J.; Mazumder, J. Pulsed laser deposition of hydroxyapatite thin films on Ti–6Al–4V: Effect of heat treatment on structure and properties. *Acta Biomater.* **2009**, *5*, 1821–1830. [CrossRef]
42. Blind, O.; Klein, L.H.; Dailey, B.; Jordan, L. Characterization of hydroxyapatite films obtained by pulsed-laser deposition on Ti and Ti-6AL-4v substrates. *Dent. Mater.* **2005**, *21*, 1017–1024. [CrossRef]
43. Arias, J.L.; Mayor, B.; Pou, J.; Rehman, I.; Knowles, J.; Best, S.; Bonfield, W.; García, F.; León, B.; Pérez-Amor, M. Effect of heat treatment on pulsed laser deposited amorphous calcium phosphate coatings. *J. Biomed. Mater. Res.* **1998**, *43*, 69–76.
44. Gomes, G.; Borghi, F.; Ospina, R.; López, E.; Borges, F.; Mello, A. Nd: YAG (532 nm) pulsed laser deposition produces crystalline hydroxyapatite thin coatings at room temperature. *Surf. Coat. Technol.* **2017**, *329*, 174–183. [CrossRef]
45. Yuan, B.; Chen, H.; Zhao, R.; Deng, X.; Chen, G.; Yang, X.; Xiao, Z.; Aurora, A.; Iulia, B.A.; Zhang, K.; et al. Construction of a magnesium hydroxide/graphene oxide/hydroxyapatite composite coating on Mg–Ca–Zn–Ag alloy to inhibit bacterial infection and promote bone regeneration. *Bioact. Mater.* **2022**, *18*, 354–367. [CrossRef] [PubMed]
46. Hidalgo-Robatto, B.; López-Álvarez, M.; Azevedo, A.; Dorado, J.; Serra, J.; Azevedo, N.; González, P. Pulsed laser deposition of copper and zinc doped hydroxyapatite coatings for biomedical applications. *Surf. Coat. Technol.* **2018**, *333*, 168–177. [CrossRef]
47. Ungureanu, E.; Dragomir, A.V.; Parau, A.C.; Mitran, V.; Cimpean, A.; Tarcolea, M.; Vranceanu, D.M.; Cotrut, C.M. In Vitro Evaluation of Ag- and Sr-Doped Hydroxyapatite Coatings for Medical Applications. *Materials* **2023**, *16*, 5428. [CrossRef] [PubMed]
48. Prodan, A.M.; Iconaru, S.L.; Predoi, M.V.; Predoi, D.; Motelica-Heino, M.; Turculet, C.S.; Beuran, M. Silver-Doped Hydroxyapatite Thin Layers Obtained by Sol-Gel Spin Coating Procedure. *Coatings* **2020**, *10*, 14. [CrossRef]
49. Cao, Z.; Li, L.; Yang, L.; Yao, L.; Wang, H.; Yu, X.; Shen, X.; Yao, L.; Wu, G. Osteoinduction Evaluation of Fluorinated Hydroxyapatite and Tantalum Composite Coatings on Magnesium Alloys. *Front. Chem.* **2021**, *9*, 727356. [CrossRef]
50. Zhang, L.; Liu, W.; Yue, C.; Zhang, T.; Li, P.; Xing, Z.; Chen, Y. A tough graphene nanosheet/hydroxyapatite composite with improved in vitro biocompatibility. *Carbon* **2013**, *61*, 105–115. [CrossRef]
51. Cotrut, C.M.; Ungureanu, E.; Ionescu, I.C.; Zamfir, R.I.; Kiss, A.E.; Parau, A.C.; Vladescu, A.; Vranceanu, D.M.; Saceleanu, A. Influence of Magnesium Content on the Physico-Chemical Properties of Hydroxyapatite Electrochemically Deposited on a Nanostructured Titanium Surface. *Coatings* **2022**, *12*, 1097. [CrossRef]
52. Nistor, L.; Ghica, C.; Teodorescu, V.; Nistor, S.; Dinescu, M.; Matei, D.; Frangis, N.; Vouroutzis, N.; Liutas, C. Deposition of hydroxyapatite thin films by Nd: YAG laser ablation: A microstructural study. *Mater. Res. Bull.* **2004**, *39*, 2089–2101. [CrossRef]
53. Yashiro, H.; Kakehata, M. A High-Quality Hydroxyapatite Layer Coated by Droplets Eliminated the Pulsed-Laser Deposition Scheme. In *Laser Applications in Microelectronic and Optoelectronic Manufacturing (LAMOM) XXVIII*; SPIE: Bellingham, WA, USA, 2023.
54. Yashiro, H.; Kakehata, M. High crystalline hydroxyapatite coating by eclipse type pulsed-laser deposition for low annealing temperature. *Appl. Phys. Lett.* **2022**, *120*, 131602. [CrossRef]
55. Lin, K.C.; Chiu, Y.H.; Lin, J.H.; Pai, W.W. A quantitative analysis of the shape transition of Ge islands on Si(100) with NC-AFM. *Nanotechnology* **2005**, *16*, S63–S67. [CrossRef]
56. Popa, A.; Stan, G.; Enculescu, M.; Tanase, C.; Tulyaganov, D.; Ferreira, J. Superior biofunctionality of dental implant fixtures uniformly coated with durable bioglass films by magnetron sputtering. *J. Mech. Behav. Biomed. Mater.* **2015**, *51*, 313–327. [CrossRef] [PubMed]
57. ISO 13779-2:2018; Implants for surgery—Hydroxyapatite—Part 2: Thermally Sprayed Coatings of Hydroxyapatite. Available online: <https://www.iso.org/standard/64617.html> (accessed on 19 September 2023).
58. ASTM D4541; Standard Test Method for Pull-Off Strength of Coatings Using Portable Adhesion Testers. ASTM: West Conshohocken, PA, USA, 2017.
59. ISO 4624; Paints and varnishes—Pull-off test for adhesion. ISO: Geneva, Switzerland, 2016.
60. Bäuerle, D. *Laser Processing and Chemistry*; Springer Science & Business Media: Berlin/Heidelberg, Germany, 2013.
61. Chen, L.-C.; Chrisey, D.; Hubler, G. *Pulsed Laser Deposition of Thin Films*; Wiley: New York, NY, USA, 1994.
62. Kautek, W.; Roas, B.; Schultz, L. Formation of Y-Ba-Cu-oxide thin films by pulsed laser deposition: A comparative study in the UV, visible and IR range. *Thin Solid Film.* **1990**, *191*, 317–334. [CrossRef]
63. Liu, H.; Mao, X.; Yoo, J.; Russo, R. Early phase laser induced plasma diagnostics and mass removal during single-pulse laser ablation of silicon. *Spectrochim. Acta Part B At. Spectrosc.* **1999**, *54*, 1607–1624. [CrossRef]
64. Ojeda-G-P, A.; Döbeli, M.; Lippert, T. Influence of Plume Properties on Thin Film Composition in Pulsed Laser Deposition. *Adv. Mater. Interfaces* **2018**, *5*, 1701062. [CrossRef]
65. Agop, M.; Cimpoesu, N.; Gurlui, S.; Irimiciuc, S.A. Investigations of Transient Plasma Generated by Laser Ablation of Hydroxyapatite during the Pulsed Laser Deposition Process. *Symmetry* **2020**, *12*, 132. [CrossRef]
66. Mayor, B.; Arias, J.; Chiussi, S.; Garcia, F.; Pou, J.; Fong, B.L.; Pérez-Amor, M. Calcium phosphate coatings grown at different substrate temperatures by pulsed ArF-laser deposition. *Thin Solid Film.* **1998**, *317*, 363–366. [CrossRef]
67. Abdisarov, B.; Ilhom, S.; Kholikov, K.; Loomis, D.; Dobrokhoto, V.; Khennner, M.; Er, A.O. Morphology and structure of Pb thin films grown on Si(111) by pulsed laser deposition. *Appl. Phys. A* **2020**, *126*, 1–7. [CrossRef]
68. Segal, L.; Creely, J.J.; Martin, A.E., Jr.; Conrad, C.M. An Empirical Method for Estimating the Degree of Crystallinity of Native Cellulose Using the X-Ray Diffractometer. *Text. Res. J.* **1959**, *29*, 786–794. [CrossRef]
69. Murphy, B.; Baez, J.; Morris, M.A. Characterizing Hydroxyapatite Deposited from Solution onto Novel Substrates in Terms of Growth Mechanism and Physical Chemical Properties. *Mater. Proc.* **2023**, *14*, 34.

70. Duta, L.; Mihailescu, N.; Popescu, A.C.; Luculescu, C.R.; Mihailescu, I.N.; Çetin, G.; Gunduz, O.; Oktar, F.N.; Popa, A.C.; Kuncser, A.; et al. Comparative physical, chemical and biological assessment of simple and titanium-doped ovine dentine-derived hydroxyapatite coatings fabricated by pulsed laser deposition. *Appl. Surf. Sci.* **2017**, *413*, 129–139. [[CrossRef](#)]
71. Dong, X.; Wang, Q.; Wu, T.; Pan, H. Understanding Adsorption-Desorption Dynamics of BMP-2 on Hydroxyapatite (001) Surface. *Biophys. J.* **2007**, *93*, 750–759. [[CrossRef](#)]
72. May, R.M.; Hoffman, M.G.; Sogo, M.J.; Parker, E.A.; O'toole, A.G.; Brennan, A.B.; Reddy, S.T. Micro-patterned surfaces reduce bacterial colonization and biofilm formation in vitro: Potential for enhancing endotracheal tube designs. *Clin. Transl. Med.* **2014**, *3*, 8. [[CrossRef](#)]

Disclaimer/Publisher's Note: The statements, opinions and data contained in all publications are solely those of the individual author(s) and contributor(s) and not of MDPI and/or the editor(s). MDPI and/or the editor(s) disclaim responsibility for any injury to people or property resulting from any ideas, methods, instructions or products referred to in the content.